Karadeniz Fen Bilimleri Dergisi
The Black Sea Journal of Sciences
DOI: 10.31466/kfbd.1699462
ISSN (Online): 2564-7377
https://dergipark.org.tr/tr/pub/kfbd
Research Article / Araştırma Makalesi

Determination of Control Parameters of a Bidirectional Dual Active Bridge DC-DC Converter Using Metaheuristic Algorithms

Metasezgisel Algoritmalar Kullanılarak İki Yönlü Çift Aktif Köprülü DA-DA Dönüştürücünün Kontrol Parametrelerinin Belirlenmesi

Emirhan YETER[1]*, Yahya DANAYİYEN[2]

Abstract

This study proposes an optimization approach based on metaheuristic algorithms to improve the control performance of a bidirectional dual active bridge (DAB) DC-DC converter. DAB converters are widely preferred in many applications due to their high efficiency, flexible control, and bidirectional power transfer capabilities. However, accurate determination of controller parameters is critical for achieving efficient energy transfer and minimizing losses. In this study, the DAB converter is controlled using proportional-integral (PI) and fractional-order proportional-integral (FOPI) controller structures. The controller parameters are optimized using Dandelion Optimization (DO), Particle Swarm Optimization (PSO), and Grey Wolf Optimization (GWO) algorithms, with the Integrated Time-Weighted Absolute Error (ITAE) employed as the objective function. In addition, the effects of circuit parameter selection on system efficiency are investigated. The results provide a comparative evaluation of the three algorithms and confirm the effectiveness of metaheuristic optimization in improving DAB converter control performance, contributing a comprehensive perspective to the existing literature.

Keywords: Bidirectional dual active bridge DC-DC converter, PI controller, FOPI controller, metaheuristic algorithm, particle swarm optimization (PSO), dandelion optimization (DO), grey wolf optimization (GWO), ITAE.

Öz

Bu çalışma, çift yönlü çift aktif köprülü (DAB) DA-DA dönüştürücünün kontrol performansını iyileştirmek amacıyla metasezgisel algoritmalara dayalı bir optimizasyon yaklaşımı önermektedir. DAB dönüştürücüler, yüksek verimleri, esnek kontrol yapıları ve çift yönlü güç aktarım kabiliyetleri nedeniyle birçok uygulamada yaygın olarak tercih edilmektedir. Ancak, denetleyici parametrelerinin doğru belirlenmesi, verimli enerji aktarımının sağlanması ve kayıpların en aza indirilmesi açısından kritik öneme sahiptir. Bu çalışmada, DAB dönüştürücü oransal-integral (PI) ve kesirli mertebeli oransal-integral (FOPI) denetleyici yapıları kullanılarak kontrol edilmiştir. Denetleyici parametreleri, Dandelion Optimization (DO), Parçacık Sürü Optimizasyonu (PSO) ve Gri Kurt Optimizasyonu (GWO) algoritmaları kullanılarak, amaç fonksiyonu olarak Entegre Zaman Ağırlıklı Mutlak Hata (ITAE) kriteri temelinde optimize edilmiştir. Ayrıca, devre parametrelerinin seçiminin sistem verimi üzerindeki etkileri incelenmiştir. Elde edilen sonuçlar, üç algoritmanın karşılaştırmalı bir değerlendirmesini sunmakta ve metasezgisel optimizasyonun DAB dönüştürücü kontrol performansını iyileştirmedeki etkinliğini ortaya koyarak literatüre kapsamlı bir bakış açısı kazandırmaktadır.

Anahtar Kelimeler: İki yönlü çift aktif köprülü DA-DA dönüştürücü, PI denetleyici, FOPI denetleyici, metasezgisel algoritma, parçacık sürü optimizasyonu (PSO), karahindiba optimizasyonu (DO), gri kurt optimizasyonu (GWO), ITAE.

[1,2]Karadeniz Technical University, Department of Electrical and Electronics Engineering, Trabzon, Türkiye

***Corresponding Author/Sorumlu Yazar:** emirhanyeter@ktu.edu.tr

Received/Geliş: 14.05.2025 **Accepted/Kabul:** 02.01.2026 **Published/Yayın:** 06.03.2026

Yeter, E., Danayiyen, Y., (2026). Determination of Control Parameters of a Bidirectional Dual Active Bridge DC-DC Converter Using Metaheuristic Algorithms. *Karadeniz Fen Bilimleri Dergisi*, 16(1), 304-337. https://doi.org/10.31466/kfbd.1699462

1. Introduction

In contemporary industrial applications, bidirectional dual active bridge (DAB) DC-to-DC (direct current to direct current) converters are utilized extensively. Distinctions between DAB converters and other DC-DC converters are primarily characterized by three key features: high efficiency, flexibility, and bidirectional controlled energy transfer in various application areas. In addition, these systems can operate under high power density, switch at zero voltage and current, and have self-isolation. Increasing efficiency, reducing switching losses and improving dynamic performance of DAB converters have been a major focus of power electronics research in recent years.

The first modeling studies in this field were conducted after 1990 (De Doncker et al., 1991; Kheraluwala et al., 1992). These studies serve as a crucial reference point for the investigation of DAB converters' performance at elevated power levels and the verification of bidirectional power flow. To date, DAB converters have been utilized in a variety of fields, including electric vehicles, storage systems, and energy conversion systems. A study was conducted to analyze the effects of the isolated and non-isolated status of the DAB converter used in electric vehicle (EV) batteries on power flow, efficiency, switching losses, and battery current-voltage fluctuations (Zgheib et al., 2017; He et al., 2017). The determination of the optimal dimensional parameters for the DC coupling capacitor DC within the EV charging system is a critical aspect for the functionality of the system. In this direction, a low-frequency charging current method was proposed to reduce the volume of the DC coupling capacitor in electric vehicle battery chargers. This method was experimentally verified to reduce the size of the capacitor by up to 84% (Xue et al., 2015). Krismer and Kolar (2010) developed a different power loss model for electric vehicles and showed that zero voltage switching plays a critical role in reducing switching losses. DAB converters are benefited in a variety of vehicles, including aircraft and ground vehicles. In their study, Jiang and Liu (2021) proposed a highly efficient intermittent parallel bidirectional Dual Active Bridge converter for aircraft. The proposed structure has demonstrated to facilitate a doubling of power transfer in comparison with conventional DAB converters. This enhancement is achieved by augmenting the transformer input voltage. Another area in which DAB topologies are frequently used is energy storage applications. The efficiency of a bidirectional DC-to-DC converter utilized for energy storage in electric vehicle battery systems was examined in a study by Chun Wang et al. (2016). In another experimental study on a 1kW prototype, it was observed that a bidirectional LLC resonant converter with automatic mode switching for energy storage systems provides higher efficiency compared to a conventional DAB converter (Jiang et al., 2015). In their experimental study, Nalamati et al. (2021) compared the performance of a proposed three-port isolated bidirectional DC-DC converter with that of a conventional DAB for multiple

battery packs. The results indicated that the proposed system exhibited several advantages, including its ability to support a greater number of batteries, optimize power flow management, and operate efficiently with a closed-loop control algorithm. The operation of DAB converters at high efficiency within the pertinent systems is contingent upon their proper design and control through the implementation of an efficient controller mechanism. In this direction, converter control is realized by using Phase Shifted Modulation (PSM) techniques (SPS, DPS, TPS, GPS, QPS) and various control methods (PID, MPC, Fuzzy, SMC, ML). The most widely used PSM techniques are Single Phase Shift (SPS), Dual Phase Shift (DPS) and Triple Phase Shift (TPS), which improve system performance by optimizing power flow (Shao et al., 2022; Hou et al., 2020; Kayaalp et al., 2016; Bai and Mi, 2008; Yan et al., 2020; Bohara et al., 2022; Krismer and Kolar, 2010; Tong et al., 2018).

Single loop current or voltage feedback control methods are conventionally employed for the regulation of the DAB converter. The current-fed control mechanism is responsible for regulating the bidirectional power transfer between two sources at the input and output of the DAB converter. Voltage feedback control regulates the output voltage under unidirectional power flow with a passive resistive load. For these two control methods, DAB converters are controlled using advanced algorithms such as model predictive control (MPC), fuzzy logic and machine learning (ML), as well as PID-based control strategies such as PI (Proportional-Integral), PID (Proportional-Integral-Derivative) and fractional order PID (FOPID) controllers (Ebad and Song, 2012; Chen et al., 2023; Muthukumar et al., 2024). In the study by Bindi et al. (2021), a comparison between PI controller and Model Reference Control (MRC) method for DAB converter was carried out. As a result of the study, the rise time of the MRC controller was determined as 1.5704 μs, while the rise time of the PI controller was obtained as 17.188 μs. When the results are analyzed in terms of percentage overshoot, the MRC controller has a percentage overshoot of 1.3376% while the PI controller has a percentage overshoot of 0.1714%. Koch et al. (2016) determined the control parameters using the Linear Matrix Inequalities (LMI) method in comparison with the conventional PI controller. In comparison with the conventional PI controller, the LMI-based PI controller reduced the overshoot from 15% to 5% and decreased the settling time from 40 ms to 20 ms. This resulted in a transient response that was approximately 50% faster. In a separate study, Eberle et al. (2023) developed a control approach to enhance the dynamic performance of DAB converters. This approach utilizes a cascade structure of PI and PID controllers. The controller parameters are determined by genetic algorithm. Another type of controller, the FOPID controller, has been shown to realize a more flexible and precise control process by working with fractional degrees of integral and derivative operations in the system (Dong et al., 2024). In this study, the design and analysis of FOPID controller for isolated bidirectional DC-DC converters are presented (Ramya et al., 2018).

The performance of DAB converters depends not only on the type of control method, but also on how accurately the parameters of this method are set. Accordingly, in order to ensure system stability and maximize performance, metaheuristic algorithms have come to the forefront in recent years as a solution tool in addition to traditional methods. Metaheuristic algorithms are advanced search and optimization techniques used to find optimal or near-optimal solutions in complex and large search spaces (Kırıkcı et al., 2024; Aksoy et al., 2024). These algorithms can be effectively applied to different problem types by providing high flexibility and adaptability in solution generation inspired by natural and physical processes (Örnek et al., 2023). A review of the extant literature reveals the existence of studies that have investigated the determination of the control parameters of the DAB converter with metaheuristic algorithms. Jia and Wang (2024) proposed a Particle Swarm Optimization (PSO)-based Dynamic Matrix Control (DMC) control method to minimize the current stress of the DAB converter. According to the results, the current stress is determined as 8.56 A under SPS-PI control and 5.95 A under DPS-PI control, while this value is reduced to 5.05 A with the proposed method. In addition, while the rise time of the output current is 103 ms under conventional PI control, this value is reduced to 19 ms under the proposed DMC control. In a different study, a Multi-Objective Genetic Algorithm (MGA-II) based method was proposed for modulation optimization in a DAB converter circuit developed for electric vehicles (Alzuguren et al., 2022). The findings indicate that the optimized modulation results in a 64% reduction in transmission losses, a 57% reduction in switching losses, and a 63% reduction in total semiconductor losses. Consequently, there is a 3.3% increase in system efficiency. Ab-Ghani et al. (2020) proposed a PSO-based phase shift angle optimization method to improve the efficiency of the DAB converter. Here, the stabilization time of the output voltage is determined as 150 ms in the absence of the algorithm, while this time is reduced to 100 ms when the PSO algorithm is applied. Du and Chen (2023) aimed to improve voltage stability in DC microgrids by optimizing PI controller parameters using Genetic Algorithms (GA). The analysis conducted in the study under a sudden load reduction scenario revealed that GA optimization reduced the maximum voltage drop to 4% from 8% for PI control, to 5% from 7.5% for SMC control, and to 0.7% from 1.0% for MPC control. Ghamari et al. (2025) proposed a new FOPID controller initiated with Grey Wolf Optimization (GWO) and adjusted in real time with Multi-Agent Reinforcement Learning (DDPG-based) for high-power DAB converters. The proposed controller demonstrated faster dynamic response compared to traditional PID controller types. Specifically, the settling time was reduced to 1.8 s and overshoot to 5%. Ruiz et al. (2024) proposed a new hybrid optimization method that combines AEO and chaotic MRFO algorithms to optimize FOPID controller parameters for DAB converters. The hybrid algorithm delivered the lowest best value of 0.0385 in IAE (Integral of Absolute Error) performance, while the lowest best value of 0.0807 was reported in ISE (Integral of Squared Error) performance. Ghamari et al. (2025)

propose a new robust adaptive cascade control strategy integrated into a CLLC-filtered structure for use in high-power DAB converters for electric vehicle applications. The internal current loop is controlled by an Adaptive Backstepping Controller (ABSC), while the external voltage loop is controlled by an FOPID. The gains of both controllers are optimized using the Grey Wolf Optimization (GWO) algorithm. The results show that the controller reduces the settling time to 1.5–2.0 s and the overshoot to 2% in both boost and buck modes.

Existing literature reviews clearly show that studies on the use of metaheuristic algorithms in determining the optimal control parameters of DAB converters are limited. Furthermore, it is observed that the improvements achieved with existing optimization approaches are not sufficiently satisfactory, particularly in terms of dynamic performance and overshoot values. Studies reported in the literature highlight that both PI and FOPI-based control structures have long settling times and significant overshoot values. Within the scope of this article, the parameters of PI and FOPI controllers were determined using Dandelion Optimization (DO), Particle Swarm Optimization (PSO), and Grey Wolf Optimization (GWO) algorithms to improve the controllability and dynamic performance of the DAB converter. The study provides a comprehensive comparative analysis by evaluating all algorithms under equal conditions and details the effects of different optimization methods on control performance. The findings contribute significantly to the literature by comparatively analyzing the effects of both PI and FOPI controllers and the metaheuristic algorithms used on the performance of the DAB converter. In particular, the analyses clearly show which algorithms are more stable, faster, and achieve lower overshoot values. In addition, the DAB converter structure has been examined in detail theoretically, and important evaluations regarding the converter design have been included through the three-dimensional analyses performed. Furthermore, the selection of circuit parameters and the effects of changes in these parameters on system efficiency have been examined in detail. The findings obtained are valuable as a reference for academic studies. The remainder of the paper is organized as follows. Section 2 provides a comprehensive examination of the DAB converter and its associated control mechanisms. The performance analysis and simulation results of the system are discussed in Section 3. The conclusions are presented in Section 4.

2. Materials and Methods

The enhancement of DAB DC-DC converter performance and the assurance of optimal operating conditions are contingent upon the accurate specification of the parameters. However, the stability and power transfer efficiency of the system are contingent upon the modulation technique employed, the controller parameters, and the characteristics of the circuit elements. In this chapter,

the fundamental operating principles of the DAB converter and the methodologies that ensure the efficient operation of the system are discussed in detail.

2.1. DAB DC-DC Converter

Current industrial and automotive DC power supplies are anticipated to possess the capability to regulate the direction of power flow. The DAB converter circuit, which enables the flow of power between two bridge circuits fed from two distinct sources, is depicted in Figure 1. In this particular type of power electronic circuit, the forward power flow is initiated from source V_1, which supplies the first bridge, and continues to source V_2, which supplies the second bridge. The reverse power flow is in the opposite direction, from V_2 supplying the second bridge to V_1 supplying the first bridge.

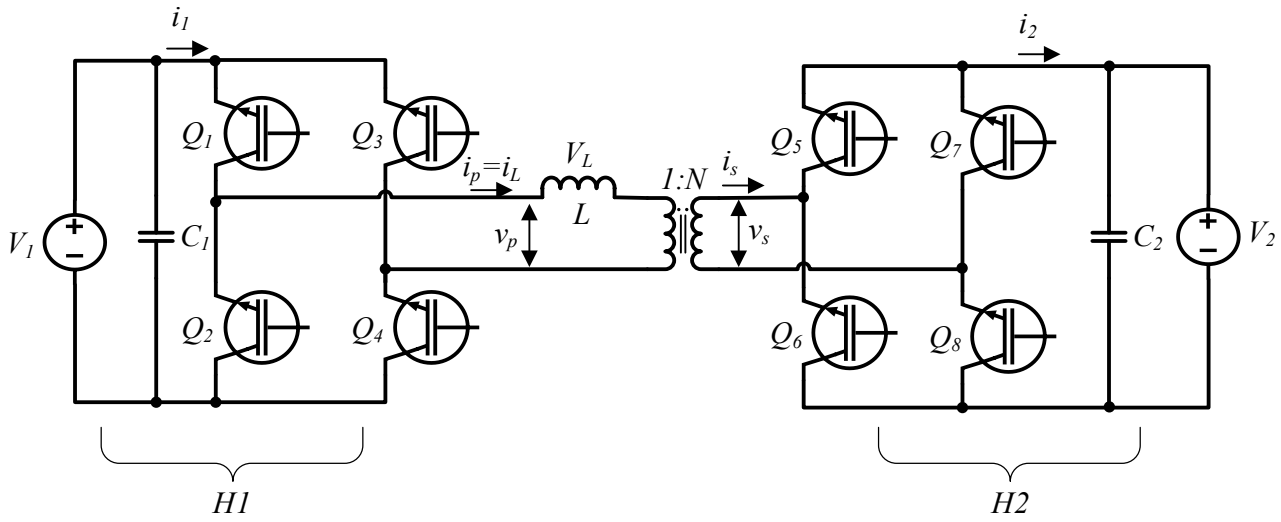

Figure 1. Circuit configuration of DAB converter.

When the voltage source V_1, which is one of the two sources in the DAB converter circuit depicted in Figure 1, exceeds the voltage source V_2, the primary end of the transformer with N windings constitutes the high voltage side, while the secondary end forms the low voltage side. Additionally, given the bidirectional nature of the DAB, it follows that either of the two active bridges (*H1, H2*) comprising the circuit can function as either an input or an output. A salient feature of the DAB converter circuit is that it consists of two active bridges with four semiconductor switches each, which are connected by a transformer. The high frequency transformer provides electrical isolation between the two sources. In addition to its function of providing isolation to the DAB converter circuit, the transformer can be utilized to obtain different voltage conversion ratios. The *H1* and *H2* bridges that make up the converter circuit work exactly opposite to each other. The transformer requires AC voltage at the primary and secondary ends. Therefore, the *H1* bridge, to which the

primary end of the transformer is connected, acts as an inverter by converting the DC voltage obtained from the V_1 voltage source into AC voltage. Conversely, the *H2* bridge, to which the secondary end of the transformer is connected, acts as a rectifier by converting the AC voltage received from the transformer into a DC voltage. For a simpler analysis of the DAB converter circuit, the secondary side of the converter must be referred to the primary side. Accordingly, the quantities are changed to $v_s' = Nv_s$, $i_s' = i_s/N$, $V_2' = NV_2$ and $C_2' = C_2/N^2$. Here *N* represents the transformer conversion ratio. The expressions for the two voltage sources given in Figure 1 are given in Equation 1.

$$V_1(t) = V_1 cos(\omega t) \quad , \quad V_2(t) = V_2 cos(\omega t - \phi) \tag{1}$$

Where V_1 and V_2 are the effective values of the source voltages, ω is the source angular frequency and ϕ is the phase difference between the two source voltages. The power flow direction is from the first source to the second source for $\phi > 0$ and from the second source to the first source for $\phi < 0$. For the case $\phi > 0$, the average power supplied by the first source to the circuit and the average power absorbed by the second source are given in Equation 2 and Equation 3.

$$P_1 = \frac{1}{T}\int_0^T v_1(t) i_1(t) dt \tag{2}$$

$$P_2 = \frac{1}{T}\int_0^T v_2(t) i_2(t) dt \tag{3}$$

Where, $T = 1/f$ is the period value and f is the source frequency. To express the instantaneous time-dependent values, the voltage and current magnitudes are shown as v_1, v_2, i_1, i_2. In the case where losses are neglected, the average power supplied by the first source is completely absorbed by the second source. In this case, $P_1 = P_2$. The current value in the power expressions given in Equation 2 and Equation 3 is obtained by Equation 4.

$$i_2(t) = \frac{V_1}{\omega L} sin(\omega t) - \frac{V_2}{\omega L} sin(\omega t - \phi) \tag{4}$$

If the expression given in Equation 4 is substituted into the power equation in Equation 3, Equation 5 is obtained as follows.

$$P_2 = \frac{1}{T}\int_0^T \left(V_2 cos(\omega t - \phi) \left(\frac{V_1}{\omega L} sin(\omega t) - \frac{V_2}{\omega L} sin(\omega t - \phi) \right) \right) dt \tag{5}$$

If the expressions in Equation 5 are calculated with trigonometric identities, the output power P_2 is as in Equation 6.

$$P_2 = \frac{V_1 V_2}{\omega L} sin\phi \tag{6}$$

The expression given in Equation 6 refers to the average power transferred between two voltage sources. The average power is contingent upon the phase difference. The value of the transferred power can be controlled by utilizing the value of the phase difference. The controller has the capacity to modify the value of the transmitted power by altering the phase difference. This control mechanism has been demonstrated to enhance the flexibility and efficiency of the DAB converter, thereby facilitating stable power transfer under varying load conditions. The theoretical explanations provided above elucidate the fundamental operational principle of the DAB converter and the manner in which power transfer is modulated by phase difference. For the system to function optimally, it is imperative that the components of the circuit be appropriately sized. The next section discusses the process of determining the circuit parameters that directly affect the performance of the converter.

2.2. Determination of Circuit Parameters

Before determining the circuit parameters in single phase DAB converter, finding the average transmitted power will facilitate the parameter determination. The transmitted power expression is given in Equation 7.

$$P_{2,avg} = I_{2,avg} V_2 \tag{7}$$

Here, the average value of the output current ($I_{2,avg}$) must be found to calculate the transmitted power. The graphical representation of i_2' obtained by reducing the secondary side of the DAB converter to the primary side is given in Figure 2. $I_{2,avg}$ is obtained by calculating the area under the graph.

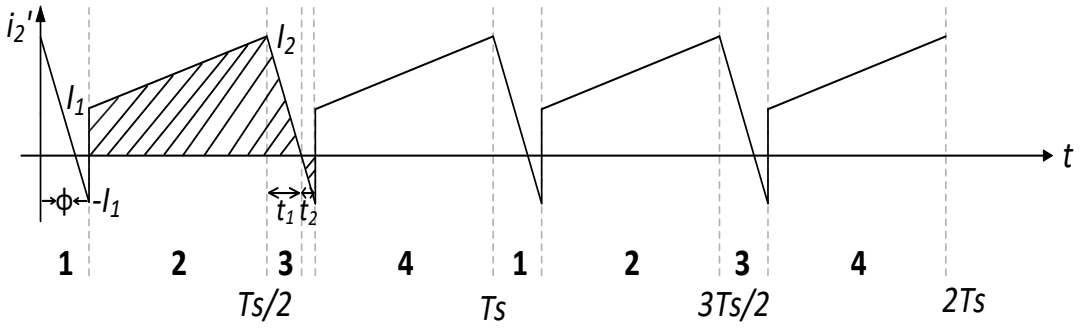

Figure 2. DAB converter output current.

As illustrated in the output current graph, the formation of positive and negative areas transpires within a single period. The hatched area below the output current graph, consisting of positive and negative regions, is the load variation, denoted as ΔQ. The value of ΔQ provides the average current value ($I_{2,avg}$) in the transmitted power formula given in Equation 7. The value of the expression $I_{2,avg}$ for the average current is shown as follows:

$$I_{2,avg} = \frac{\Delta Q}{\frac{T_S}{2}} \tag{8}$$

In Equation 8, the ΔQ value refers to the area under the given output current graph. In this case, the mathematical calculation of the given area is given in Equation 9. In addition, the values of t_1 and t_2 in Equation 9 need to be calculated. For this, Equation 10 and Equation 11 are used.

$$\Delta Q = \frac{1}{2}(I_1 + I_2)\left(\frac{T_s}{2} - t_\phi\right) + \frac{1}{2}I_2 t_1 - \frac{1}{2}I_1 t_2 \tag{9}$$

$$t_1 = \frac{I_2 L}{V_1 + \frac{V_2}{N}} \tag{10}$$

$$t_2 = \frac{I_1 L}{V_1 + \frac{V_2}{N}} \tag{11}$$

If the expressions given in Equation 10 and Equation 11 are substituted into Equation 9, Equation 12 is formed.

$$\Delta Q = \frac{1}{2}(I_1 + I_2)\left(\frac{T_s}{2} - t_\phi\right) + \left(\frac{\frac{1}{2}I_2^2}{\frac{V_1 + \frac{V_2}{N}}{L}}\right) - \left(\frac{\frac{1}{2}I_1^2}{\frac{V_1 + \frac{V_2}{N}}{L}}\right) \tag{12}$$

The expression for ΔQ given by Equation 12 is more simply written as follows.

$$\Delta Q = t_\phi \left(\frac{T_S}{2} - t_\phi\right)\left(\frac{V_1}{L}\right) \tag{13}$$

If the expression given by Equation 13 is substituted in Equation 8 and $t_\phi = D\frac{T_S}{2}$ is transformed, the average value of the $I_{2,avg}$ in Equation 14 is obtained.

$$I_{2,avg} = \frac{V_1 D(1-D)}{2NLf_S} \tag{14}$$

Where D is the phase shift value. The effective ($I_{L,rms}$) and peak ($I_{L,peak}$) value expressions of i_L current are given in Equation 15 and Equation 16 respectively.

$$I_{L,rms} = \sqrt{\frac{1}{3}\left(i_1^2 + i_2^2 + \left(1 - \frac{2\varphi}{\pi}\right) i_1 i_2\right)} \tag{15}$$

$$I_{L,peak} = 0.5|I_{\text{base}}(D\varphi - \pi D - \varphi + \pi)| \tag{16}$$

The current expressions i_1 and i_2 at the input and output of the DAB converter are described in detail in Equation 17 and Equation 18. I_{base} is the reference current value used to analyze the current flowing through L in the DAB converter and is defined as $I_{base} = \frac{V_1}{2\pi f_S L}$ depending on the circuit parameters.

$$i_1 = 0{,}5(2\varphi - (1-D)\pi) I_{base} \tag{17}$$

$$i_2 = 0{,}5(2D\varphi + (1-D)\pi) I_{base} \tag{18}$$

To facilitate a more nuanced comprehension of these relationships, a graphical analysis is employed to elucidate the impact of leakage inductance (L) and switching frequency (f_s) on the system. Figure 3 presents the contour plot illustrating the impact of f_s and L parameters on $I_{L,rms}$ and $I_{L,peak}$ values. The contour plot was generated using Equations 15 and 16. It is an important reference for determining the optimum operating parameters of the converter.

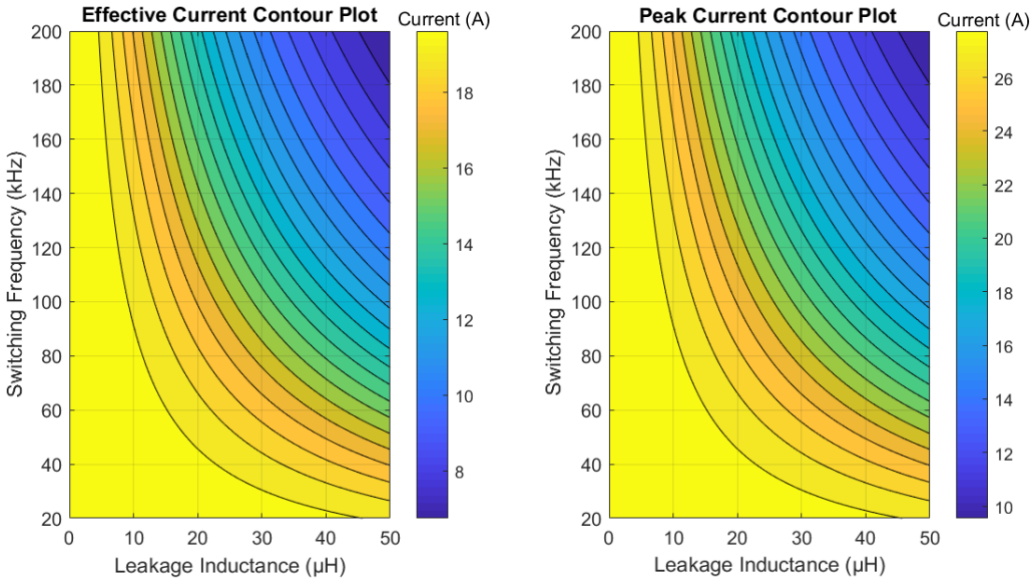

Figure 3. Effect of L and f_s parameters on i_L.

As demonstrated in Figure 3, with an increase in L, both $I_{L,rms}$ and peak $I_{L,peak}$ values of the inductance current undergo a decrease. As L values decrease, the current values concomitantly increase, thereby exerting greater current stress on the converter. Conversely, as f_s increases, the current magnitudes decrease for a given L value. In the low-value range of L, the value of the inductance current (i_L) demonstrates an upward trend in conjunction with an increase in f_s. In scenarios where both L and f_s parameters undergo an increase, i_L undergoes a decrease. Thus, despite the increase in switching losses at high f_s, the thermal load is reduced by decreasing the current levels. Thermal load, defined as the heat accumulation resulting from power losses in switching elements and magnetic components, is a crucial consideration in the analysis of energy dissipation in electrical systems. Accordingly, the current magnitudes, which vary with the values of L and f_s, directly affect not only the thermal behavior but also the output characteristics of the converter. Given that $I_{2,avg}$ is equal to V_2/R, P_2 is given in Equation 19.

$$P_{2,avg} = \frac{V_1 V_2 D(1-D)}{2NLf_s} \tag{19}$$

The value of N in Equation 19 is calculated by Equation 20 below.

$$N = \frac{V_1}{V_2} \tag{20}$$

The parameters D and L are related to the transmitted power expression given in Equation 19. If the converter is required to operate over a wide power range, the value of L should be calculated

with Equation 21. Here the maximum phase shift (D_{max}) should be 0.4. In the other case, if the converter is required to provide maximum efficiency at full load, the L value should be calculated with Equation 22. Here the minimum phase shift value $D_{min} = 0.1$ should be taken.

$$L = \frac{NV_1V_2D_{max}(1-D_{max})}{2f_sP_{2,max}} \tag{21}$$

$$L = \frac{NV_1V_2D_{min}(1-D_{min})}{2f_sP_{2,max}} \tag{22}$$

The interrelationship among L, D_{max} and V_1 is examined through the three-dimensional surface plot depicted in Figure 4. As demonstrated in this analysis, the L parameter is directly influenced by alterations in the D_{max} and V_1 values. Specifically, as D_{max} diminishes, a substantial decline in the L value is observed. For example, when $D = 0.2$ to achieve a lower L, the leakage inductance value becomes $L = 25\ \mu H$. On the other hand, when $D = 0.4$ is chosen for a higher L value, the leakage inductance is calculated as $L = 36\ \mu H$. Similarly, an increase in the value of L is observed with increasing V_1. This indicates that the leakage inductance will be higher at higher input voltages and lower at lower input voltages. In order to obtain the optimum value of L, the parameters V_1 and D_{max} need to be thoroughly analyzed.

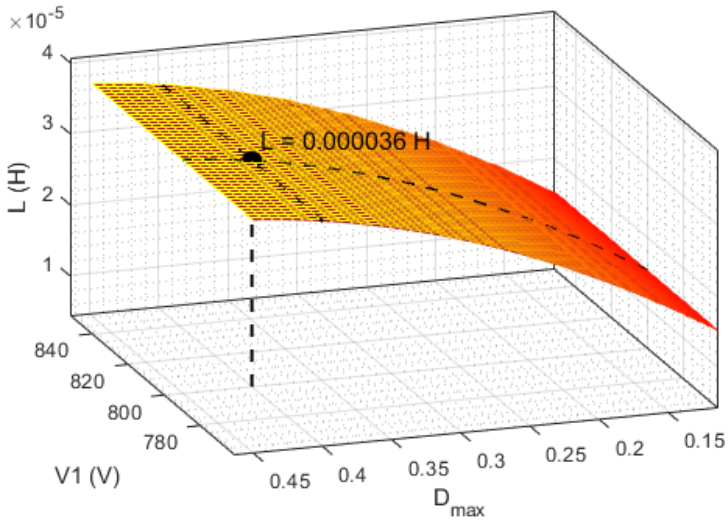

Figure 4. Variation of the parameter L depending on V_1 and D.

After evaluating the effects of leakage inductance on system performance, the value of the output capacitor, which is another critical design parameter, needs to be determined. In order to keep the output voltage ripple (ΔV_2) within the desired limits, the minimum capacitor value must be calculated depending on the other parameters in the system. In the case where the voltages V_1 and V_2

are assumed constant, the required capacitor value is expressed by Equation 23, which is based on the D_{max} for the minimum capacitance (C_2).

$$C_2 \geq \frac{1}{\Delta V_2}\frac{NV_1}{4f_s^2 L}\left(D^2\left(1-D+\frac{1}{4}D^2\right)\right)\Big|_{D=D_{max}} \tag{23}$$

The relationship between C_2, V_1 and ΔV_2 is analyzed with the three-dimensional surface plot given in Figure 5. Here, C_2 varies directly with V_1 and inversely with ΔV_2. The situation observed in the graph is theoretically consistent with the mathematical inequality given by Equation 23. As ΔV_2 increases, C_2 decreases. This indicates that the choice of large value capacitors will minimize ΔV_2. On the other hand, it can be seen from the figure that C_2 increases as the V_1 increases in the DAB converter. This shows that in applications where high input voltages are used, larger capacitors should be used to control the output voltage fluctuations.

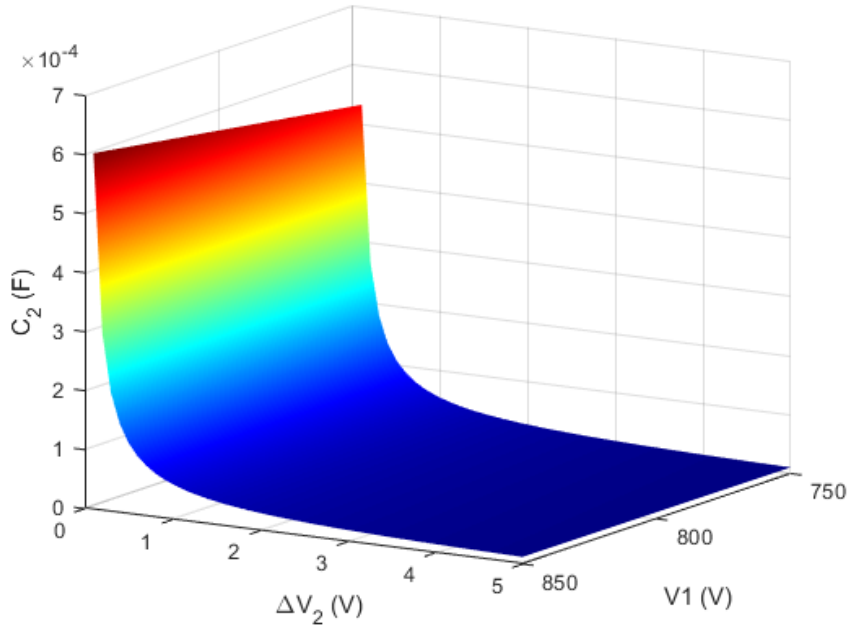

Figure 5. Variation of parameter C_2 depending on V_1 and ΔV_2.

Figure 6 is obtained by adding the parameter L to the plot of C_2 versus V_1 and ΔV_2 given in Figure 5. As illustrated in Figure 6, the color-coded surfaces demonstrate the variation in capacitance values for different inductance values ranging from 18 µH to 90 µH. As demonstrated, the quantity ΔV_2 undergoes a decrease with the rise in C_2. Conversely, an increase in C_2 results in an augmentation of both size and cost. For larger L values, smaller C_2 values are obtained to achieve the same voltage ripple. As the load increases, the capacitor values become more stable, and the sensitivity to voltage variations decreases. As can be seen in Figure 6, C_2 decreases as the leakage inductance value

increases. For example, when $L = 90\mu H$, $C_2 = 200\,\mu F$. On the other hand, when $L = 18\,\mu H$ for higher C_2 value, $C_2 = 1300\,\mu F$. Here, the relationship between C_2 and L is shaped according to Equation 23. When the necessary calculations are made in Equation 23, the optimum C_2 value is obtained. In DAB converters with low leakage inductance, a larger output capacitor is required, while in systems with high leakage inductance, smaller capacitors are sufficient.

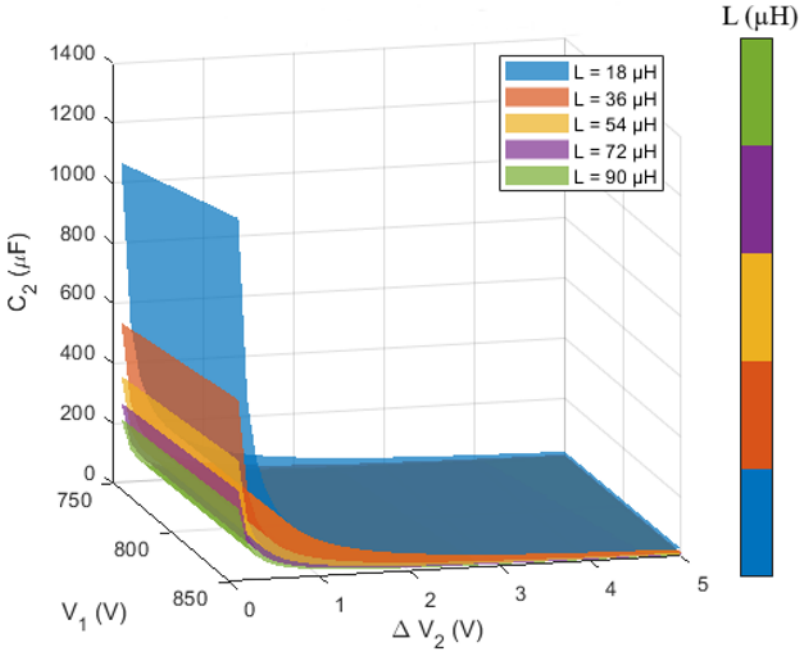

Figure 6. C_2 behavior for different values of L.

2.3. PI Controller

To ensure the stability of the system and to minimize the output power fluctuations, depending on the parameter values used in the DAB converter circuit, effective control of the converter is required. The objective of this control process is to attain the desired stable operating conditions by decreasing the fluctuations of the output current and, consequently, the output power. In this context, the PI controller with two different parameters (K_p and K_i), whose block diagram is given in Figure 7, regulates the dynamic response of the system using a combination of proportional and integral components and significantly increases the stability. The PI controller is designed to regulate the control variable ($U(s)$) in order to minimize the error signal ($E(s)$) between the reference value and the measured value (Chincholkar et al., 2024). This process is intended to optimize system performance.

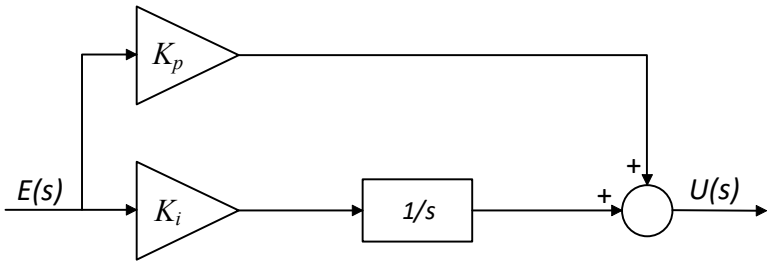

Figure 7. Block diagram of the PI controller.

Where K_p represents the proportional gain constant and K_i the integral gain constant. The transfer function G_{PI} of the PI controller is given in Equation 24.

$$G_{PI} = K_p + \frac{K_i}{s} \tag{24}$$

2.4. FOPI Controller

In contrast to the classical PI controller, the FOPI controller utilizes a fractional degree (λ) in the integral gain (K_i). This approach engenders a more adaptable control strategy for the system. This feature, in addition to enhancing the system's dynamic performance, offers a more comprehensive control mechanism (Qi et al., 2020). The FOPI controller, as depicted in Figure 8, perpetually observes the error signal ($E(s)$) between the reference value and the measured value, with the objective of minimizing this discrepancy (Thaliyadath et al., 2024). The system under consideration comprises three distinct parameters: proportional gain (K_p), integral gain (K_i), and fractional integral degree (λ).

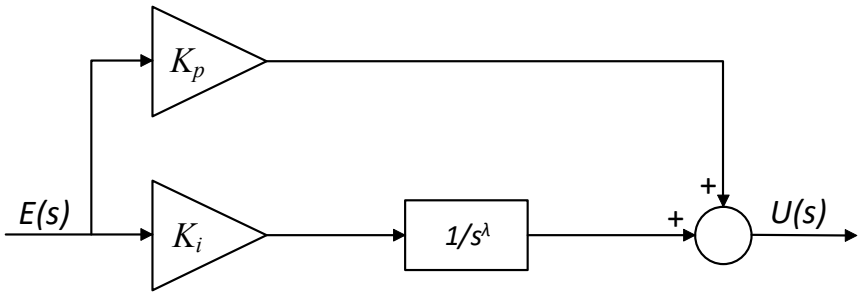

Figure 8. Block diagram of the FOPI controller.

Where K_p is the proportional gain constant, K_i is the integral gain constant and λ is the fractional integral degree. The transfer function G_{FOPI} of the FOPI controller is given in Equation 25.

$$G_{FOPI} = K_p + \frac{K_i}{s^{\lambda}} \tag{25}$$

In this study, the control of the DAB converter is realized with PI and FOPI controllers. The determination of optimal controller parameters is achieved through the implementation of DO, PSO, and GWO algorithms. The following subsections provide a comprehensive analysis of the utilized algorithms.

2.5. Algorithms

To ensure the stability of the system and to minimize the output power fluctuations, effective control of the converter is required. This control process reduces the fluctuations of the output current and, consequently, the output power, thereby achieving the desired stable operating conditions. Metaheuristic algorithms have gained popularity due to their problem solving capabilities in many fields. Inspired by nature, these algorithms aim to identify solutions that approximate the global optimum by drawing inspiration from biological, physical, or social systems (Kırıkcı et al., 2024; Ieng et al., 2025; Danayiyen et al., 2024). Their extensive range of applications enables them to produce highly accurate and efficient solutions, providing an effective approach to solving complex problems. Figure 9 shows the relationship between the DAB converter and the algorithms.

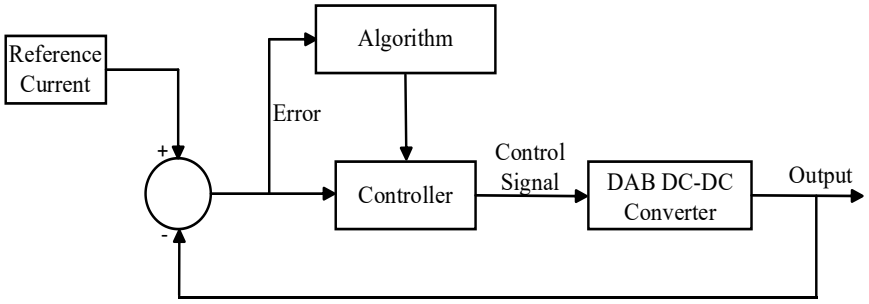

Figure 9. Algorithm-system block diagram.

2.5.1. Dandelion Optimization (DO)

The DO algorithm is a swarm intelligence-based optimization method that draws inspiration from natural phenomena. The algorithm generates a balanced exploration and exploitation mechanism in the solution space by modeling the dispersal of dandelion seeds carried by wind to random locations (Zhao et al., 2022). The DO is comprised of three distinct phases: ascent, expansion, and descent. These phases constitute the large area exploration, uniform distribution of solutions and determination of the optimum solution parts of the algorithm, respectively. In the ascent phase, the dandelion seeds rise spirally under the influence of air currents and drag forces. The movement

exhibited by the particles is proportional to the wind speed, which is considered to follow a log-normal distribution (Öztürk and Çavdar, 2024). Thus, seeds are capable of being transported over greater distances. This stage is mathematically defined in Equation 26.

$$X_{t+1} = X_t + \alpha v_x v_y \ln Y \, (X_s - X_t) \tag{26}$$

Where X_t is the current position at iteration t, X_s is a random search space position, $\ln Y$ is a log-normal distribution and α is a parameter that determines the search step length. At this stage of optimization, the probability of dandelion seeds being carried over long distances by the wind increases. The random motion driven by the wind is given in Equation 27. Here $rand$ is a random number generator.

$$\alpha = rand\left(\frac{1}{T^2}t^2 - \frac{2}{T}t + 1\right) \tag{27}$$

In the subsequent phase, the initial phase, the seeds commence their dispersal, following a predetermined trajectory from the altitude at which they have accumulated. Since this is modeled by Brownian motion, the seeds have a more controlled distribution. As delineated in Equation 28, the search direction is determined by calculating the average position of the population. Subsequently, in Equation 29, the position of each seed is updated.

$$X_{mean,t} = \frac{1}{pop}\sum_{i=1}^{pop} x_i \tag{28}$$

$$X_{t+1} = X_t - \alpha\beta_t\left(X_{mean,t} - \alpha\beta_t X_t\right) \tag{29}$$

Where, β_t is a random value that determines Brownian motion. In the final stage, the landing stage, the seeds land in specific locations and enter the growth process. In this process, the best solution (X_{elite}) is determined using Levy flight. The update expression of the best solution is given in Equation 30 and the mathematical representation of the Levy flight is given in Equation 31.

$$X_{t+1} = X_{elite} - levy(\lambda)\alpha(X_{elite} - X_t\delta) \tag{30}$$

$$levy(\lambda) = s\frac{\omega\alpha}{|t|^{1/\beta}} \tag{31}$$

Where β is a random number in the interval $[0,2]$, s is a small constant value, ω and t are random numbers.

2.5.2. Particle Swarm Optimization (PSO)

PSO algorithm was first proposed by Kennedy and Eberhart (1995) and was inspired by the behavior of flocks of birds, fish, and other animals as they adapt to their environment, search for food sources, and avoid predators (Liu, 2023; Derin et al., 2024). Here, the solution-seeking particles are influenced by both their own experiences and the collective behavior of the swarm. The algorithm is initialized with a certain number of randomly generated particles and these particles are updated to determine the optimal solution value. Each particle is updated using its own best solution (p_{best}) and the best solution of all particles (g_{best}). The motion of the particles is determined by the velocity update equation given in Equation 32.

$$v_i^{k+1} = w_i v_i^k + c_1 rand \times \left(pbest_i - x_i^k\right) + c_2 rand \times \left(gbest - x_i^k\right) \quad (32)$$

Where v_i^{k+1} is the velocity of particle i at iteration k, w_i is the inertia weighting factor, $rand$ is a random number between 0 and 1, c_1 and c_2 are the acceleration coefficients, $pbest_i$ is the best position that the current particle has reached so far, $gbest$ is the global best position obtained by all informants and x_i^k is the position of particle i at iteration k. The new position of each particle is given in Equation 33 and the inertial weight factor (w_i) is given in Equation 34.

$$x_i^{k+1} = x_i^k + v_i^{k+1} \quad (33)$$

$$w_i = w_{max} - \frac{w_{max} - w_{min}}{iter_{max}} \times iter \quad (34)$$

Where, $iter_{max}$ represents the maximum number of iterations, $iter$ represents the current number of iterations, w_{max} and w_{min} represent the upper and lower bounds of the inertia weight factor, respectively.

2.5.3. Grey Wolf Optimization (GWO)

GWO algorithm is a metaheuristic algorithm developed by Seyedali Mirjalili and Andrew Lewis (Mirjalili et al., 2014). The algorithm models the hunting behavior of grey wolves and performs exploration and exploitation processes in the solution space in a balanced manner (Hocaoğlu et al., 2023). In this context, the optimization process is facilitated by the hierarchical structure that exists

among four distinct grey wolf species, designated Alpha, Beta, Delta, and Omega. Equation 35 illustrates the position vectors that denote the location of the grey wolves.

$$\vec{D}_{(\alpha,\beta,\delta)} = \left|\vec{C}_{(1,2,3)}\, \vec{X}_{(\alpha,\beta,\delta)}(t) - \vec{X}(t)\right| \tag{35}$$

Equation 36 determines the positions of the new Omega wolves, as follows.

$$\vec{X}_{(1,2,3)} = \vec{X}_{(\alpha,\beta,\delta)}(t) - \vec{A}_{(1,2,3)}\vec{D}_{(\alpha,\beta,\delta)} \tag{36}$$

Where, $\vec{D}_{(\alpha,\beta,\delta)}$ is the vectorial distance between grey wolves and prey, $\vec{X}_{(\alpha,\beta,\delta)}$ is the vectorial position of the prey for grey wolves, and $\vec{X}(t)$ is the position of the grey wolf at iteration t. The vectors $\vec{C}_{(1,2,3)}$ representing the random movement fields of grey wolves and $\vec{A}_{(1,2,3)}$ representing the constant multiplier vector are given in Equation 37 and Equation 38 respectively.

$$\vec{C}_i = 2\,\vec{r}_2 \quad , \quad i = 1,2,3 \ldots \tag{37}$$

$$\vec{A}_i = |2a\,\vec{r}_1 - a| \quad , \quad i = 1,2,3 \ldots \tag{38}$$

Where a is a constant coefficient that can take values between $[0, 2]$. $\vec{r}_1$ and $\vec{r}_2$ are randomly generated vectors. The position update for all wolves is given in Equation 39.

$$\vec{X}(t+1) = \frac{\vec{X}_1 + \vec{X}_2 + \vec{X}_3}{3} \tag{39}$$

2.6. Objective Function

In metaheuristic algorithms, the choice of an appropriate objective function is critical. The objective function guides the search process toward optimal or near-optimal solutions in complex, high-dimensional problem domains. This function employs quantitative analysis to evaluate each candidate solution, facilitating a systematic comparison of alternative solutions and incremental enhancement of performance. In control-oriented applications, this function needs to accurately reflect the system behavior in terms of both transient and steady-state performance. In this study, the Time Weighted Absolute Error Integral (ITAE) is chosen as the objective function. The ITAE function is chosen because it has the property of penalizing persistent errors more than sudden errors.

This property makes it suitable for dynamic systems like DAB converters, where error damping and responsiveness are important for controller tuning. The ITAE function given in Equation 40 is given.

$$ITAE = \int_0^t t|e(t)|dt \tag{40}$$

3. Findings and Discussion

A simulation model of the DAB DC-DC converter was created in the MATLAB environment, and the simulation results were analyzed by adding PI and FOPI controllers to the system. Three distinct metaheuristic algorithms are employed to ascertain the PI and FOPI control parameters, and the outcomes are subsequently compared. For each metaheuristic algorithm, the number of iterations and population size were set to 100 and 50, respectively. For all optimization algorithms, the controller parameters were constrained as $0 < K_p < 5$, $500 < K_i < 10000$, and $0 < \lambda < 1$ to ensure a fair and feasible optimization process. The nominal parameters of the simulated model are enumerated in Table 1.

Table 1. DAB converter parameters in the simulation.

Quantity	Symbol	Value
Input voltage	V_1	800 V
Output voltage	V_2	450 V
Output current	I_1	22 A
Output power	P_1	10 kW
Leakage inductance	L	76.8 µH
Switching frequency	f_s	100 kHz
Phase shift	D	-0.4 ≤ φ ≤ 0.4 (rad)
Turn ratio	N	1.77
Output capacitance	C_2	453.33 µF

The parameters in Table 1 are given for a 10 kW DAB converter with constant input and output voltage. When $V_1 = 800\,\text{V}$ and $V_2 = 450\,\text{V}$, the N value is calculated as 1.77 using Equation 20. Another parameter in the simulation model, L, is calculated using Equation 21 for a wide power range and a value of 76.8 µH is obtained. The C value was determined as 453.33 µF using Equation 23. The DAB converter built using the parameters in Table 1 was controlled by the SPS method. The graphs showing the phase difference between v_p and v_s voltages of the transformer in the DAB converter are given in Figure 10.

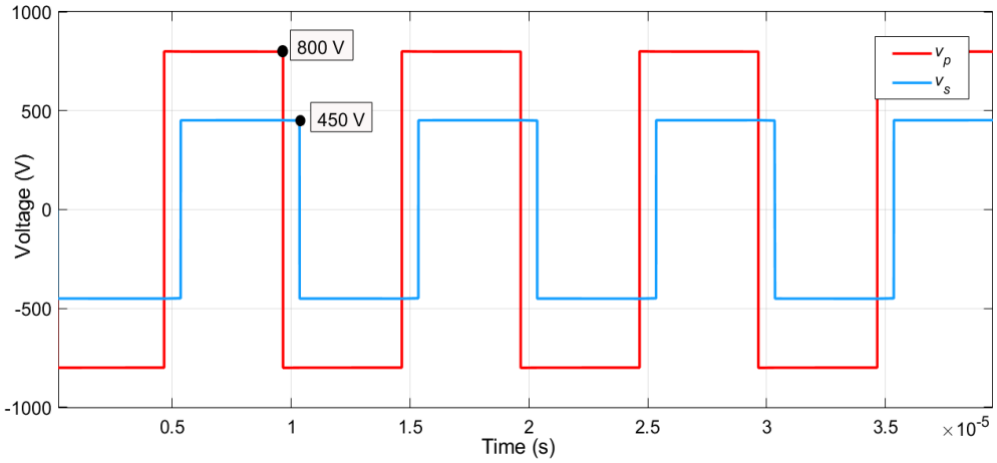

Figure 10. Transformer primary and secondary voltages in DAB converter.

L is a pivotal component of the DAB, determining the amount of power transferred ($P_{2,avg}$) and the transfer time. The accurate determination of L is imperative to ensure that the output current waveform attains the desired level. This enhancement leads to an improvement in the efficiency of power transfer and the overall performance of the system. When the output power expression of the DAB given in Equation 19 is analyzed, it is seen that there is an inversely proportional relationship between L and $P_{2,avg}$. To support this mathematical relationship, the dynamic effect of L on $P_{2,avg}$ has been tested in a simulated environment. As illustrated in Figure 11, the time-dependent change in the output power of the DAB converter varies with different L values. Notably, at an L-value of 40 µH, the output power reaches approximately 8.5 kW and demonstrates a rapid dynamic response. Also, when an inductance with $L = 120$ µH is used, the output power decreases approximately 2.8 kW. This indicates that increasing the inductance limits the energy transfer rate.

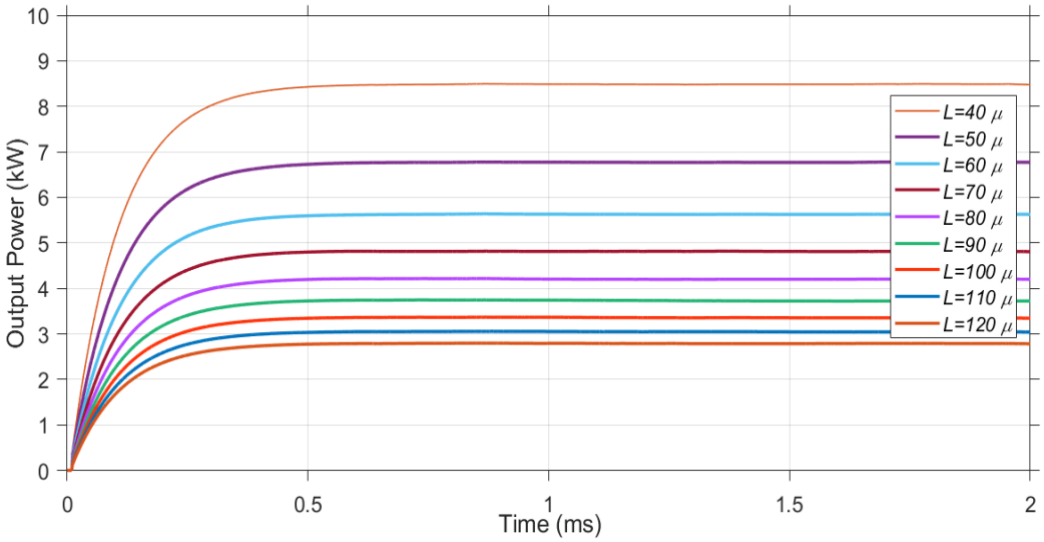

Figure 11. P_2 plots for different values of L.

In the DAB converter circuit, fluctuations in the output voltage occur in a certain range due to changes in load current and the effect of non-ideal circuit elements. The C_2 parameter is employed to ensure that these fluctuations remain within acceptable limits. Increasing the capacitor value increases the damping ratio of the output voltage fluctuations. However, if a value significantly higher than the optimal capacitor value is selected, distortions in the output voltage may occur. As demonstrated in Equation 23, there is a decline in ΔV_2 with rising C_2. To establish the basis for this relationship, a test was conducted in a simulated environment to determine the effect of C_2 on ΔV_2. The output voltage fluctuations for different capacitor values are obtained and the values of the fluctuations are given in Table 2. As can be seen, the fluctuation in the output voltage decreases with increasing capacitance value. For a capacitance of 50 µF, the voltage fluctuation is 1.3844 V, while for a capacitance of 500 µF, the fluctuation decreases to 1.1100 V. When the capacitance value is between 750 µF and 1000 µF, the ripple in the output voltage continues to show a significant decrease. However, at 1250 µF and other capacitance values the ripple becomes much more limited. Since the ripple difference between 1000 µF and 2000 µF is quite small, a balance between cost, size and performance must be struck to select the optimum capacitor value.

Table 2. ΔV_2 values for different C_2.

C_2	ΔV_2
50 µF	1.3844
100 µF	1.2603
250 µF	1.1327
500 µF	1.1100
750 µF	1.1077
1000 µF	1.1069
1250 µF	1.1065
1500 µF	1.1063
1750 µF	1.1063
2000 µF	1.1063

The switching frequency (f_s) is a pivotal parameter that influences the output power (P_2) and efficiency (η) of the DAB converter. Equation 19 demonstrates an inverse relationship between f_s and P_2. Thus, the selection of f_s value should be optimized in accordance with a specific P_2 target. Accordingly, the effect of different f_s values on the output power is shown in Figure 12. As shown in the graphs in the figure, the value of P_2 in the DAB converter decreases with increasing f_s. For instance, at a frequency of $f_s = 100$ kHz, the output power reaches a maximum of approximately 10 kW. Conversely, at $f_s = 400$ kHz, P_2 declines below 2 kW, thereby achieving the minimum power

transfer. These results indicate that high f_s values should not be preferred in terms of system efficiency and power transfer capacity.

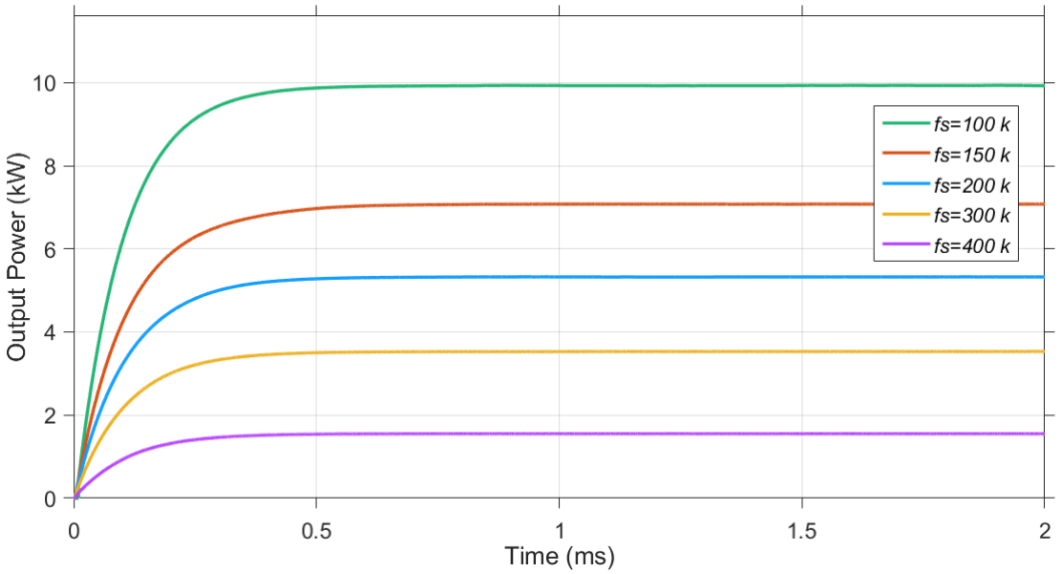

Figure 12. P_2 plots for different values of f_s.

Table 3 shows the comparative performance of the PI controller on the output current parameter of the DAB converter. The control parameters (K_p, K_i) for the PI controller were determined using three different metaheuristic algorithms. The performance indicators enumerated in the table are listed as peak value (I_{peak}), rise time (t_r), settling time (t_s), and percentage overshoot ($\%M_p$). In this study, the optimal PI controller parameters were obtained using three different metaheuristic optimization algorithms. The DO algorithm yielded optimal gains of $K_p = 0.927771$ and $K_i = 9919.367952$. Similarly, the PSO algorithm resulted in $K_p = 0.891147$ and $K_i = 9942.806691$, while the GWO produced optimal values of $K_p = 0.868694$ and $K_i = 9961.394536$. According to the results, $t_r = 0.0058\,s$ and $t_s = 0.0246\,s$ for all three algorithms. This finding suggests that there is no time-dependent change in the dynamic response of the system. However, a notable disparity is evident in the I_{peak} and $\%M_p$ values of the system when comparing the algorithms. The PSO algorithm has the lowest $\%M_p$ value with 2.3501%. On the other hand, the GWO algorithm obtained the lowest I_{peak} value with 20.0310 A. According to the results obtained, it is seen that while a more balanced and controlled system response is obtained with the PSO, the GWO algorithm exhibits a more aggressive dynamic behavior.

Table 4 shows the comparative performance of the FOPI controller on the I_2 parameter of the DAB converter. The control parameters (K_p, K_i and λ) for the FOPI controller are determined using three different metaheuristic algorithms. For the FOPI controller, the optimal control parameters were determined using three different metaheuristic optimization algorithms. The DO algorithm achieved

optimal values of $K_p = 0.943915$, $K_i = 9995.172948$, and $\lambda = 0.707030$. In comparison, the PSO algorithm yielded $K_p = 0.929636$, $K_i = 8983.065313$, and $\lambda = 0.695316$, whereas the GWO resulted in $K_p = 1.347019$, $K_i = 8809.653497$, and $\lambda = 0.749019$. These variations in the proportional gain, integral gain, and fractional order highlight the differing exploration–exploitation capabilities of the applied algorithms in tuning the FOPI controller. The values of t_r and t_s are obtained as $t_r = 0.0638\ s$ and $t_s = 0.0645\ s$ for all algorithms. This finding indicates that the respective algorithms offer analogous transient response characteristics and do not induce a substantial time-dependent variation in the dynamic response of the controller. With regard to the I_{peak} and $\%M_p$ parameters of the system, the GWO algorithm demonstrated the most optimal outcomes. In this context, $I_{peak} = 28.7800$ A value is obtained and it is observed that the GWO algorithm performs the best in terms of reducing the current stress in the system. In addition, the GWO algorithm achieved the lowest overshoot rate with a value of $\%M_p = 3.4335$, making it the best performing algorithm in this parameter. This finding indicates that the GWO algorithm facilitates a more balanced and controlled system response compared to other algorithms in determining the parameters (K_p, K_i and λ) of the FOPI controller utilized in DAB converter control. In general, the PI controller structure produced lower I_{peak} values compared to the FOPI controller. However, it is observed that it provides a more consistent and controlled system response, especially in terms of $\%M_p$ and t_s. These results show that PI controllers provide a more precise and balanced control in DAB converter applications.

Table 3. System performance results for PI controller.

Algorithms	I_{peak} (A)	t_r (s)	t_s (s)	M_p (%)
DO	23.1430	0.0058	0.0246	3.0454
PSO	23.3208	0.0058	0.0246	2.3501
GWO	23.0310	0.0058	0.0246	3.2132

Table 4. System performance results for FOPI controller.

Algorithms	I_{peak} (A)	t_r (s)	t_s (s)	M_p (%)
DO	32.2905	0.0638	0.0645	3.7216
PSO	32.2165	0.0638	0.0645	3.6614
GWO	28.7800	0.0638	0.0645	3.4335

The results obtained from 20 runs of the algorithms using PI and FOPI controllers were statistically analyzed according to the ITAE objective function. For each algorithm, the best value,

average value, and standard deviation were calculated to evaluate performance stability and consistency. This analysis reveals not only the algorithms' ability to reach the best solution but also their reliability under multiple runs. The statistical data obtained is presented comparatively in Table 5. The lowest error value for the PI controller was obtained by the DO and PSO algorithms (0.0002625). Although the DO algorithm demonstrated a more stable performance compared to other methods with a very low standard deviation value of 2.38×10^{-7}. The PSO algorithm, on the other hand, has a higher average error value (0.0002642) and standard deviation (2.50×10^{-6}). The GWO algorithm has the highest average error (0.0002723) and largest standard deviation (9.34×10^{-6}) values, showing the lowest stability in the PI controller. Regarding the FOPI controller results, the DO algorithm again showed the most stable performance with the lowest average error (0.0002420) and smallest standard deviation (1.60×10^{-5}) values. Although the PSO algorithm achieved a good error value of 0.0002348, its high average value (0.0002757) indicates an imbalance in the solution distribution. The GWO algorithm, on the other hand, produced the weakest result in the FOPI controller with both the highest average error (0.0003263) and the largest standard deviation (4.71×10^{-5}). In general, the DO algorithm demonstrated the most balanced and reliable optimization performance for both types of controllers, with the lowest error and smallest standard deviation values.

Table 5. Statistical analysis for metaheuristic algorithms.

	PI			FOPI		
Algorithms	The Best Value	Mean Value	Standard Deviation	The Best Value	Mean Value	Standard Deviation
DO	0.0002625	0.0002626	2.38E-07	0.0002253	0.0002420	1.60E-05
PSO	0.0002625	0.0002642	2.50E-06	0.0002348	0.0002757	3.44E-05
GWO	0.0002636	0.0002723	9.34E-06	0.0002542	0.0003263	4.71E-05

Figure 13, Figure 14 and Figure 15 show the P_2 plots of the DAB converter according to the PI controller parameters (K_p, K_i) determined using DO, PSO and GWO algorithms. The fluctuations observed in the output power graphs are attributed to various factors such as magnetic circuit parameters, control strategy and the time required for switching between on-off states of the switching elements. According to the obtained graphs, $t_r = 0.0058\,s$ and $t_s = 0.0646\,s$ for all three algorithms. This shows that there is no time-dependent change in the dynamic response of the system. In the P_2 results of the system, significant differences were observed between the algorithms in $\%M_p$ values. As seen in Figure 13, when the PI controller optimized with the DO algorithm (DO-PI) is used, $\%M_p = 3.0470$ is obtained. When the PI controller optimized with the PSO algorithm (PSO-

PI) is used in Figure 14, this value is obtained as $\%M_p = 2.3172$. On the other hand, the value of $\%M_p = 3.2181$ is obtained with the PI controller optimized with the GWO algorithm (GWO-PI) in Figure 15. The findings indicate that the PSO-PI controller yields the lowest percentage of $\%M_p$. Furthermore, the P_2 graphs obtained with DO-PI and GWO-PI demonstrate a substantial fluctuation subsequent to the system's attainment of steady state. This finding indicates that DO-PI and GWO-PI controllers are ineffective in damping high-frequency vibrations. The fact that the steady state P_2 value is quite smooth shows that the PSO algorithm optimizes the PI controller parameters in the best way and provides the most stable control performance by reducing the fluctuations.

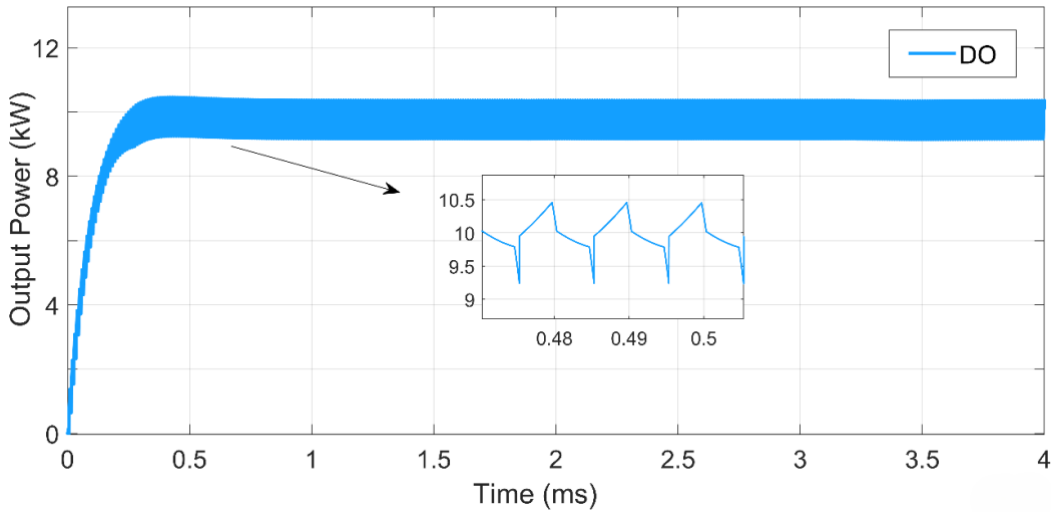

Figure 13. DAB Output Power with DO-PI Control.

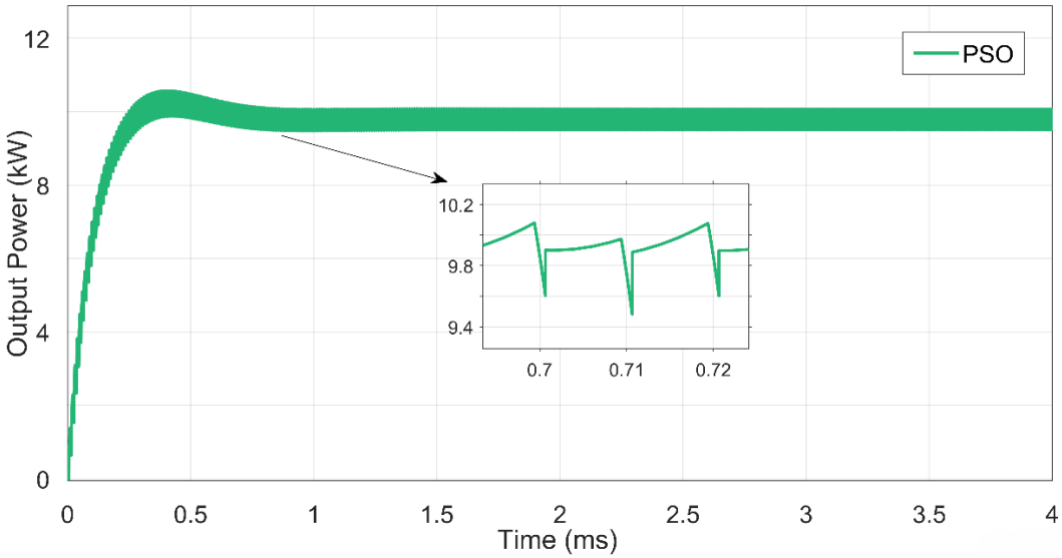

Figure 14. DAB Output Power with PSO-PI Control.

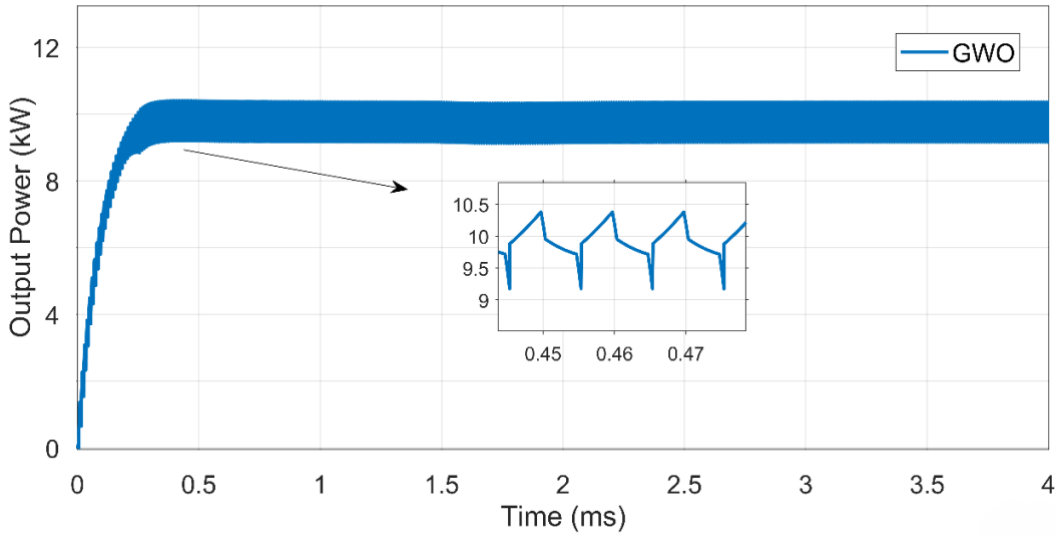

Figure 15. DAB Output Power with GWO-PI Control.

Figure 16, Figure 17 and Figure 18 show the P_2 plots of the DAB converter according to the FOPI controller parameters (K_p, K_i, λ) determined using DO, PSO and GWO algorithms. The obtained plots show that $t_r = 0.0638\ s$ and $t_s = 0.0645\ s$ for all three algorithms. This indicates that the algorithms provide similar transient response characteristics. As seen in Figure 16, the value of $\%M_p = 3.7123$ is obtained when the FOPI controller (DO-FOPI) optimized with the DO algorithm is used. When the FOPI controller optimized with the PSO algorithm (PSO-FOPI) is used in Figure 17, this value is obtained as $\%M_p = 3.6523$. However, the value of $\%M_p = 3.4249$ was obtained with the FOPI controller optimized with the GWO algorithm (GWO-FOPI) in Figure 18. Here, the lowest value in terms of $\%M_p$ is provided by the GWO-FOPI controller. The GWO algorithm optimizes the FOPI controller parameters in the best way and shows the most stable control performance by reducing the fluctuations.

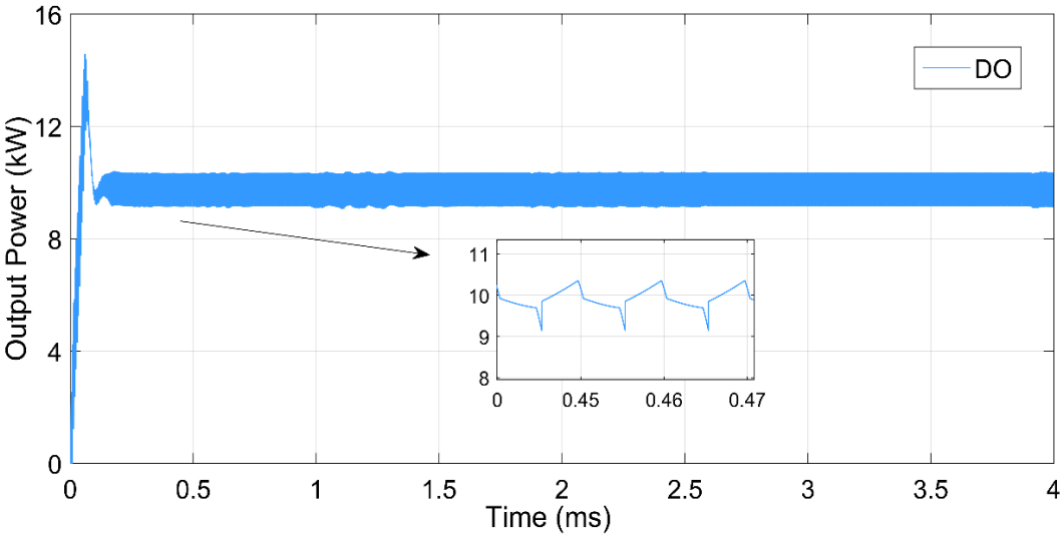

Figure 16. DAB Output Power with DO-FOPI Control.

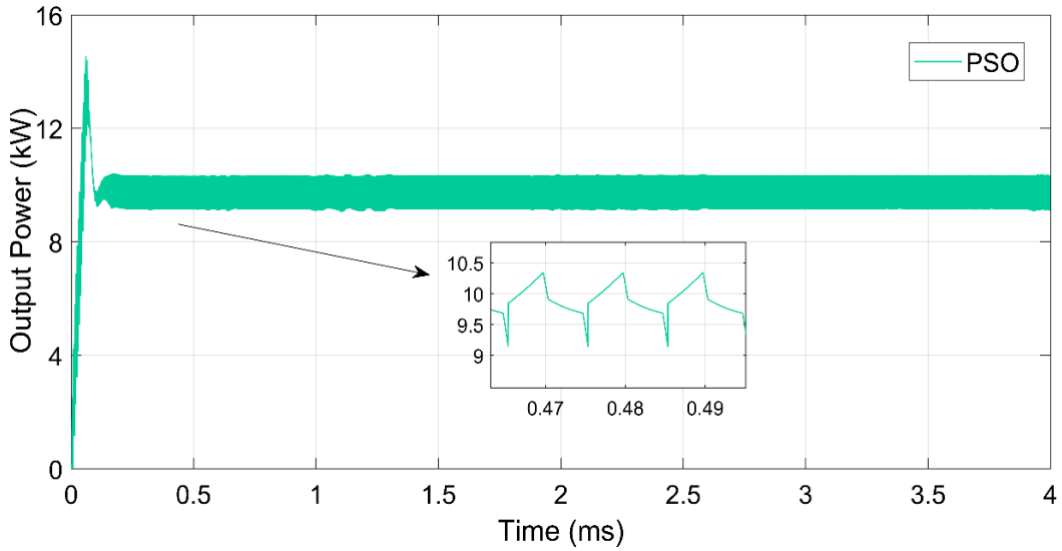

Figure 17. DAB Output Power with PSO-FOPI Control.

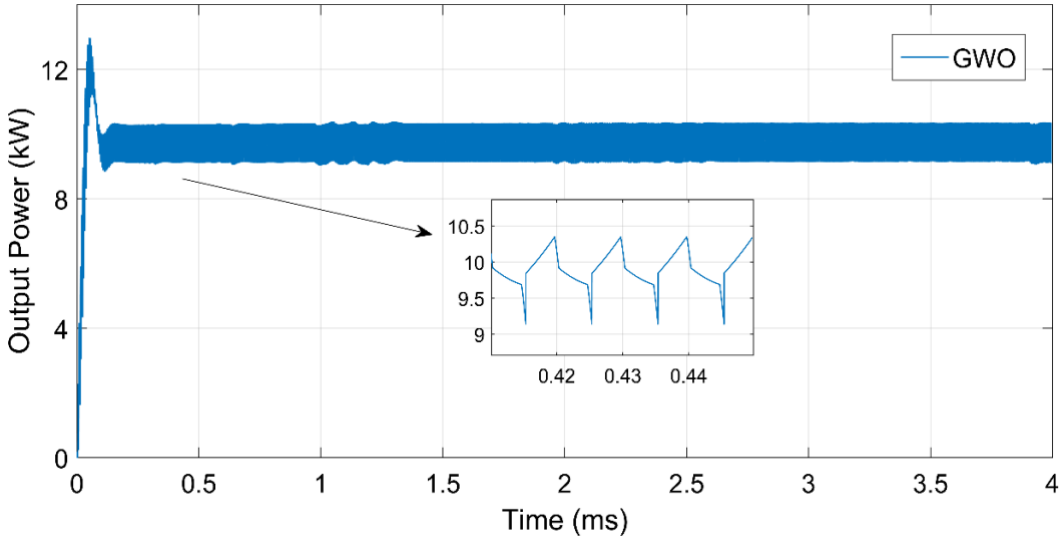

Figure 18. DAB Output Power with GWO-FOPI Control.

The findings indicate that the DAB converter controlled by the PI controller exhibits superior performance in comparison to the FOPI controller. In fact, when the results given in Table 3 and Table 4 are analyzed, the values of $t_r = 0.0058\ s$ and $t_s = 0.0246\ s$ are obtained with the relevant algorithms for the PI controller, while these values are fixed as $t_r = 0.0638\ s$ and $t_s = 0.0645\ s$ for the FOPI controller. This outcome suggests that the PI controller expedites dynamic performance by considerably diminishing transient response time. When the results are evaluated in terms of I_{peak}, the lowest value of 23.0310 A with the PI controller is obtained with the DO algorithm. Conversely, for the FOPI controller, this value is 28.7800 A, which is achieved through the implementation of the GWO algorithm. Furthermore, when evaluated in terms of $\%M_p$, the lowest overshoot rate with the PI controller was obtained with the PSO algorithm at 2.3501%, while for the FOPI controller, this rate was 3.4335% and was achieved with the GWO algorithm. In general, the PI controller stands out

with shorter transient periods (t_r, t_s), lower I_{peak} and $\%M_p$ values. On the other hand, the FOPI controller generates larger output current, potentially allowing higher energy transfer. However, this results in increased switching and transmission losses, as well as $\%M_p$. In addition, the GWO algorithm yielded the lowest I_{peak} for both controllers, while the PSO algorithm attained the lowest $\%M_p$ with the PI controller. The DO algorithm is generally more balanced but less optimized than the other algorithms. The main reason for the difference between the results obtained is that the algorithms used differ in their ability to scan the solution space and accordingly the way the controller parameters are determined. This leads to different effects of each algorithm on the system performance. In this study, PI and FOPI controllers are systematically optimized with three different metaheuristic algorithms (DO, PSO, GWO) and a detailed comparison is performed on a DAB converter. The extant literature contains a paucity of studies on such controller and algorithm combinations. In this study, numerical comparisons are presented for both transient regime (t_r, t_s and $\%M_p$) and current performance (I_{peak}), and each structure is thoroughly analyzed. In this respect, the study makes a significant contribution to the existing literature by determining the appropriate controller-optimization algorithm matching for the DAB converter.

4. Conclusions and Recommendations

In this study, the parameters of PI and FOPI controllers are determined by using different metaheuristic algorithms to optimize the control performance of a bidirectional dual active bridge DC-DC converter. The DO, PSO, and GWO algorithms are employed in the study, and the dynamic performance of the system is analyzed according to the obtained parameters. The employment of ITAE as the objective function in the optimization process ensures the system's rapid and stable convergence on the reference value. According to the simulations and performance results, it is seen that all three algorithms can determine the appropriate parameters for PI and FOPI controllers. For the PI controller, the PSO algorithm was found to be the most successful algorithm in terms of controlling the DAB converter since it provides the lowest overshoot ($\%M_p = 2.3501$) for parameter I_2 and the most stable output power characteristics. For the FOPI controller, the GWO algorithm has lower overshoot ($\%M_p = 3.4335$) and peak current value ($I_{peak} = 28.7800$ A) for parameter I_2 compared to the other algorithms.

The results presented in Table 6 provide a comprehensive comparison of the performance of the PI and FOPI controllers obtained using the proposed algorithms with similar studies in the literature. It is observed that the proposed optimization-based controllers provide significant improvements in system dynamics. In the literature, the rise time $t_r = 0.0171\ s$ and settling time

$t_s = 0.0352\ s$ were observed in the PI controller presented by Bindi et al. (2021), using the DMC method, these values were obtained as $t_r = 0.0015\ s$ and $t_s = 0.0420\ s$. However, PI controllers optimized with the metaheuristic algorithms used in the proposed study stood out with a much shorter settling time ($t_s = 0.0246\ s$) and lower overshoot percentage ($\%M_p = 2.35 - 3.21$). This result indicates that the system's settling time is shorter compared to PI-based methods in the literature.

The t_s values of $1.210\ s$ and $1.120\ s$ in the PI and PID controllers developed by Ramya and Jegathesan (2016), respectively, demonstrate that classical control methods are quite slow in terms of dynamic response. In contrast, the optimization-based PI controllers used in this study exhibited much faster response times.

In the study by Koch et al. (2016), compared to the results obtained with an LMI-based PI controller where $t_r = 0.0200\ s$, $t_s = 0.0280\ s$, and $\%M_p = 5$, the PI and FOPI controllers proposed in this study exhibited a more stable transient regime behavior with lower overshoot ($\%M_p = 2.3 - 3.7$) and similar or shorter settling times. Furthermore, the results obtained using the FOPI controller developed by Dong et al. (2024) show better performance in terms of overshoot percentage when compared to the results obtained with the FOPI-based algorithms in this study.

Table 6. Comparison of controllers used in the study with the literature.

Algorithms	t_r (s)	t_s (s)	M_p (%)
DO-PI	0.0058	0.0246	3.0454
PSO-PI	0.0058	0.0246	2.3501
GWO-PI	0.0058	0.0246	3.2132
DO-FOPI	0.0638	0.0645	3.7216
PSO-FOPI	0.0638	0.0645	3.6614
GWO-FOPI	0.0638	0.0645	3.4335
Bindi et al., 2021-PI	0.0171	0.0352	0.1714
Bindi et al., 2021-DMC	0.0015	0.0420	1.3376
Ramya and Jegathesan, 2016-PI	0.0800	1.2100	-
Ramya and Jegathesan, 2016-PID	0.0600	1.1200	-
Koch et al., 2016-PI	0.0400	0.0380	18
Koch et al., 2016-PI LMI	0.0200	0.0280	5
Dong et al., 2024-PI	0.0500	0.1500	0
Dong et al., 2024-FOPI	0.0100	0.0300	4

In general, while the rise and settling times in most controllers in the literature vary between $0.02 - 1.2\ s$, the times obtained with the algorithms proposed in this study are seen to be in the range of $0.0058 - 0.064\ s$. This indicates a significant improvement in the transient response of the system. Furthermore, when evaluated in terms of overshoot, the results obtained from this study are competitive with those reported in the literature. Therefore, the PI and FOPI controllers optimized using the DO, PSO, and GWO algorithms have achieved system responses that are competitive with the PI, PID, DMC, and LMI-based methods reported in the literature in terms of both speed and overshoot.

Furthermore, a series of parameter analyses were conducted to ascertain the optimal values of circuit elements, including L, C_2, and f_s. Consequently, the analyses have yielded a range of values that each parameter should assume in order to ensure optimal performance within the system. This proposed range of values has been derived and put forth. Thus, the dynamic performance of the DAB converter is improved, output power fluctuations are minimized, and the overall efficiency of the system is increased. The present study diverges from extant literature in its approach to multidimensional performance comparison (t_r, t_s, $\%M_p$ and I_{peak}) through the utilization of PI and FOPI controllers, alongside three distinct metaheuristic algorithms (DO, PSO, and GWO). Furthermore, the study's scope extends beyond the confines of controller optimization; it delves into the intricate interplay between circuit parameters (L, C_2, f_s) and their impact on system performance. This comprehensive examination culminates in the proposal of optimal operating ranges for these parameters. In this respect, the study provides both data for controller design and a holistic perspective on the design and optimization processes of the DAB converter.

In line with the findings obtained in this study, it is observed that controller parameter optimization with metaheuristic algorithms is a highly effective method for improving the control performance of the DAB converter. In future studies, the proposed optimization approach can be applied to different control strategies for more comprehensive comparisons. In addition, the analyses presented in this study were performed in a simulation environment, and in future studies, the real-time application capabilities of the proposed methods can be evaluated by supporting them with hardware-based validations at the experimental level.

Authors' Contributions

Emirhan YETER: Writing – original draft, Visualization, Resources, Methodology, Investigation, Simulation & software. Yahya DANAYİYEN: Writing – review & editing, Supervision; Methodological guidance; Content assessment.

Statement of Conflicts of Interest

There is no conflict of interest between the authors.

Statement of Research and Publication Ethics

The author declares that this study complies with Research and Publication Ethics.

References

Ab-Ghani, S., Daniyal, H., Jaalam, N., Saad, N. M., & Ramlan, N. H. (2022). Dynamic control and performance of dual active bridge converter based particle swarm optimization. Engineering Technology International Conference (ETIC 2022), 312–316. https://doi.org/10.1049/icp.2022.2633

Aksoy, A., Bayraklı, N., Yeter, E., & Danayiyen, Y. (2024). DC microgrid design for aircraft. 2024 Innovations in Intelligent Systems and Applications Conference (ASYU), 1–5. https://doi.org/10.1109/ASYU62119.2024.10757141

Alzuguren, I., Garcia-Bediaga, A., Avila, A., Rujas, A., & Vasic, M. (2022). Genetic algorithm-based optimized modulation for dual active bridge PFC circuit for electric vehicle application. 2022 IEEE Design Methodologies Conference (DMC), 1–5. https://doi.org/10.1109/DMC55175.2022.9906470

Bai, H., & Mi, C. (2008). Eliminate reactive power and increase system efficiency of isolated bidirectional dual-active-bridge DC–DC converters using novel dual-phase-shift control. IEEE Transactions on Power Electronics, 23(6), 2905–2914. https://doi.org/10.1109/TPEL.2008.2005103

Bindi, M., et al. (2021). Comparison between PI and neural network controller for dual active bridge converter. 2021 IEEE 15th International Conference on Compatibility, Power Electronics and Power Engineering (CPE-POWERENG), 1–6. https://doi.org/10.1109/CPE-POWERENG50821.2021.9501168

Bohara, B., Karbozov, A., & Krishnamoorthy, H. S. (2022). Triple phase shift control of dual active bridge converter using machine learning methods. 2022 IEEE Texas Power and Energy Conference (TPEC), 1–6. https://doi.org/10.1109/TPEC54980.2022.9750772

Chen, S., Zhang, G., Yu, S. S., Mei, Y., & Zhang, Y. (2023). A review of isolated bidirectional DC-DC converters for data centers. Chinese Journal of Electrical Engineering, 9(4), 1–22. https://doi.org/10.23919/CJEE.2023.000034

Chincholkar, S., Tariq, M., Poshtan, M., & Sharaf, M. (2024). Normalized Error-Based PI Controller and Its Application to the DC–DC Buck Converter. Mathematics, 12(2), 240. https://doi.org/10.3390/math12020240

Danayiyen, Y., Dincer, K., & Nuhoğlu, Y. (2024). A novel fractional order proportional integral–fractional order proportional derivative controller design based on symbiotic organisms search algorithm for speed control of a direct current motor. Electrica. https://doi.org/10.5152/electr.2024.23076

De Doncker, R. W. A. A., Divan, D. M., & Kheraluwala, M. H. (1991). A three-phase soft-switched high-power-density DC/DC converter for high-power applications. *IEEE Transactions on Industry Applications*, 27(1), 63–73. https://doi.org/10.1109/28.67533

Derin, H., Yeter, E., & Danayiyen, Y. (2024). Parçacık sürü optimizasyonu yöntemi ile denkleştirici katsayılarının bulunması. Karadeniz 13th International Conference on Applied Sciences, 545–556.

Dong, Z., Yang, P., Li, Q., Zhang, M., Chang, Y., & Wang, S. (2024). Fractional order modelling and optimal control of dual active bridge converters. Systems Science & Control Engineering, 12. https://doi.org/10.1080/21642583.2024.2347886

Du, W., & Chen, W. (2023). Genetic-Algorithm-Driven Parameter Optimization of Three Representative DAB Controllers for Voltage Stability. Applied Sciences, 13(18), 10374. https://doi.org/10.3390/app131810374

Ebad, M., & Song, B.-M. (2012). Accurate model predictive control of bidirectional DC-DC converters for DC distributed power systems. 2012 IEEE Power and Energy Society General Meeting, 1–8. https://doi.org/10.1109/PESGM.2012.6345659

Eberle, T., Jalilian, A., Weitz, N., & März, M. (2023). Performance enhancement of a dual active bridge by a genetic algorithm based routine for optimal parameters of a cascade control. 2023 IEEE Applied Power Electronics Conference and Exposition (APEC), 2767–2774. https://doi.org/10.1109/APEC43580.2023.10131136

Ghamari, S. M., Habibi, D., & Aziz, A. (2025). Robust Adaptive Fractional-Order PID Controller Design for High-Power DC-DC Dual Active Bridge Converter Enhanced Using Multi-Agent Deep Deterministic Policy Gradient Algorithm for Electric Vehicles. Energies, 18(12), 3046. https://doi.org/10.3390/en18123046

Ghamari, S., Habibi, D., Ghahramani, M., & Aziz, A. (2025). Design of a robust adaptive cascade fractional-order nonlinear-based controller enhanced using grey wolf optimization for high-power DC/DC dual active bridge converter in electric vehicles. IET Power Electronics, 18(1), e70056. https://doi.org/10.1049/pel2.70056

He, P., & Khaligh, A. (2017). Comprehensive analyses and comparison of 1 kW isolated DC–DC converters for bidirectional EV charging systems. *IEEE Transactions on Transportation Electrification*, 3(1), 147–156. https://doi.org/10.1109/TTE.2016.2630927

Hocaoğlu, G. S., Çavli, N., Kılıç, E., & Danayiyen, Y. (2023). Nonlinear convergence factor based grey wolf optimization algorithm and load frequency control. 2023 5th Global Power, Energy and Communication Conference (GPECOM), 282–287. https://doi.org/10.1109/GPECOM58364.2023.10175823

Hou, N., & Li, Y. W. (2020). Overview and comparison of modulation and control strategies for a nonresonant single-phase dual-active-bridge DC–DC converter. IEEE Transactions on Power Electronics, 35(3), 3148–3172. https://doi.org/10.1109/TPEL.2019.2927930

Ieng, S., Ang, S., Vichet, H., Cheng, H., Keo, S., & Choeung, C. (2025). Dingo optimizer for power loss minimization using optimal power flow. *GMSARN International Journal*, 19(2025), 10–18.

Jia, D., & Wang, D. (2024). Current Stress Minimization Based on Particle Swarm Optimization for Dual Active Bridge DC–DC Converter. Actuators, 13(10), 421. https://doi.org/10.3390/act13100421

Jiang, C., & Liu, H. (2021). A novel interleaved parallel bidirectional dual-active-bridge DC–DC converter with coupled inductor for more-electric aircraft. *IEEE Transactions on Industrial Electronics*, 68(2), 1759–1768. https://doi.org/10.1109/TIE.2020.3018047

Jiang, T., Zhang, J., Wu, X., Sheng, K., & Wang, Y. (2015). A bidirectional LLC resonant converter with automatic forward and backward mode transition. IEEE Transactions on Power Electronics, 30(2), 757–770. https://doi.org/10.1109/TPEL.2014.2307329

Kayaalp, İ., Demirdelen, T., Koroglu, T., Cuma, M. U., Bayindir, K. C., & Tumay, M. (2016). Original research paper. International Journal of Applied Mathematics Electronics and Computers, 4(3), 68–73. https://doi.org/10.18100/ijamec.60506

Kennedy, J., & Eberhart, R. (1995). Particle swarm optimization. Proceedings of ICNN'95 - International Conference on Neural Networks, 4, 1942–1948. https://doi.org/10.1109/ICNN.1995.488968

Kheraluwala, M. N., Gascoigne, R. W., Divan, D. M., & Baumann, E. D. (1992). Performance characterization of a high-power dual active bridge DC-to-DC converter. *IEEE Transactions on Industry Applications*, 28(6), 1294–1301. https://doi.org/10.1109/28.175280

Kirikci, F. M., Akyazi, Ö., & Kahveci, H. (2024). WSO-optimized PID controller design for SEPIC converter voltage stability. 2024 8th International Artificial Intelligence and Data Processing Symposium (IDAP), 1–6. https://doi.org/10.1109/IDAP64064.2024.10710743

Koch, G. G., et al. (2016). Design of a robust PI controller for a dual active bridge converter. 2016 12th IEEE International Conference on Industry Applications (INDUSCON), 1–6. https://doi.org/10.1109/INDUSCON.2016.7874503

Krismer, F., & Kolar, J. W. (2010). Accurate power loss model derivation of a high-current dual active bridge converter for an automotive application. *IEEE Transactions on Industrial Electronics*, 57(3), 881–891. https://doi.org/10.1109/TIE.2009.2025284

Liu, F. (2023). Design of human motion training motion capture model based on improved PSO algorithm. 2023 International Conference on Applied Intelligence and Sustainable Computing (ICAISC), 1–5. https://doi.org/10.1109/ICAISC58445.2023.10200983

Mirjalili, S., Mirjalili, S. M., & Lewis, A. (2014). Grey wolf optimizer. Advances in Engineering Software, 69, 46–61. https://doi.org/10.1016/j.advengsoft.2013.12.007

Muthukumar, P., Venkateshkumar, M., & Chin, C. S. (2024). A comparative study of cutting-edge bi-directional power converters and intelligent control methodologies for advanced electric mobility. IEEE Access, 12, 28710–28752. https://doi.org/10.1109/ACCESS.2024.3360267

Nalamati, C. S., & Gupta, R. (2020). Multi-directional power flow in three-port isolated DC–DC converter for multiple battery stacks. Turkish Journal of Electrical Engineering and Computer Sciences. https://doi.org/10.3906/elk-2003-41

Örnek, R. S., Ateş, O. K., Boğa, A. Y., & Danayiyen, Y. (2023). X-band pyramidal horn antenna directivity optimization with symbiotic organism search algorithm. 2023 5th Global Power, Energy and Communication Conference (GPECOM), 519–523. https://doi.org/10.1109/GPECOM58364.2023.10175711

Öztürk, Ö., & Çavdar, B. (2024). Otomatik gerilim regülatörü sistemi denetleyici tasarımı için meta-sezgisel algoritmaların performansı. Karadeniz Fen Bilimleri Dergisi (KFBD), 14(4), 2258–2289. https://doi.org/10.31466/kfbd.1558173

Qi, Z., Tang, J., Pei, J., & Shan, L. (2020). Fractional controller design of a DC-DC converter for PEMFC. IEEE Access, 8, 120134–120144. https://doi.org/10.1109/ACCESS.2020.3005439

Ramya, K. C., & Jegathesan, V. (2016). Comparison of PI and PID controlled bidirectional DC-DC converter systems. International Journal of Power Electronics and Drive Systems (IJPEDS), 7, 56–65. https://doi.org/10.11591/ijpeds.v7.i1.pp56-65

Ramya, K. C., Kumar, K., Rani, S. S., & Radhakrishnan, G. (2018). Design and analysis of fractional PID controller for isolated bidirectional DC-DC converter. International Journal of Engineering and Technology (UAE), 7(4), 182–185. https://doi.org/10.14419/ijet.v7i4.19.22044

Ruiz, F., Pichardo, E., Aly, M., Vazquez, E., Avalos, J. G., & Sánchez, G. (2024). A High-Performance Fractional Order Controller Based on Chaotic Manta-Ray Foraging and Artificial Ecosystem-Based Optimization Algorithms Applied to Dual Active Bridge Converter. Fractal and Fractional, 8(6), 332. https://doi.org/10.3390/fractalfract8060332

Shao, S., et al. (2022). Modeling and advanced control of dual-active-bridge DC–DC converters: A review. IEEE Transactions on Power Electronics, 37(2), 1524–1547. https://doi.org/10.1109/TPEL.2021.3108157

Thaliyadath, D., Kaliyaperumal, D., & Kolhe, M. L. (2024). Enhancing Transient Response in a DC-DC Converter for Electric Vehicle DC Fast Charging Applications Using Fractional-Order PI Control. Energies, 17(17), 4312. https://doi.org/10.3390/en17174312

Tong, A., Hang, L., Li, G., Jiang, X., & Gao, S. (2018). Modeling and analysis of a dual-active-bridge-isolated bidirectional DC/DC converter to minimize RMS current with whole operating range. IEEE Transactions on Power Electronics, 33(6), 5302–5316. https://doi.org/10.1109/TPEL.2017.2692276

Wang, C., Xiong, R., He, H., Ding, X., & Shen, W. (2016). Efficiency analysis of a bidirectional DC/DC converter in a hybrid energy storage system for plug-in hybrid electric vehicles. Applied Energy, 183, 612–622. https://doi.org/10.1016/j.apenergy.2016.08.178

Xue, L., Shen, Z., Boroyevich, D., Mattavelli, P., & Diaz, D. (2015). Dual active bridge-based battery charger for plug-in hybrid electric vehicle with charging current containing low frequency ripple. *IEEE Transactions on Power Electronics*, 30(12), 7299–7307. https://doi.org/10.1109/TPEL.2015.2413815

Yan, Y., Bai, H., Foote, A., & Wang, W. (2020). Securing full-power-range zero-voltage switching in both steady-state and transient operations for a dual-active-bridge-based bidirectional electric vehicle charger. IEEE Transactions on Power Electronics, 35(7), 7506–7519. https://doi.org/10.1109/TPEL.2019.2955896

Zgheib, R., Kamwa, I., & Al-Haddad, K. (2017). Comparison between isolated and non-isolated DC/DC converters for bidirectional EV chargers. *2017 IEEE International Conference on Industrial Technology (ICIT)*, 515–520. https://doi.org/10.1109/ICIT.2017.7913285

Zhao, S., Zhang, T., Ma, S., & Chen, M. (2022). Dandelion optimizer: A nature-inspired metaheuristic algorithm for engineering applications. Engineering Applications of Artificial Intelligence, 114, 105075. https://doi.org/10.1016/j.engappai.2022.105075